Publication Year	2020
Acceptance in OA	2025-02-07T09:16:56Z
Title	Photometric modelling and VIS-IR albedo maps of Rhea from Cassini-VIMS
Authors	FILACCHIONE, GIANRICO, CIARNIELLO, Mauro, D'AVERSA, EMILIANO, CAPACCIONI, FABRIZIO, Cerroni, Priscilla, Buratti, B.J., Clark, R.N., Stephan, K., Plainaki, C.
Publisher's version (DOI)	10.1093/mnrasl/slaa162
Handle	http://hdl.handle.net/20.500.12386/35841
Journal	MONTHLY NOTICES OF THE ROYAL ASTRONOMICAL SOCIETY. LETTERS
Volume	499

Monthly Notices
of the
ROYAL ASTRONOMICAL SOCIETY

MNRAS **499,** L62–L66 (2020)
Advance Access publication 2020 September 14

doi:10.1093/mnrasl/slaa162

Photometric modelling and VIS-IR albedo maps of Rhea from Cassini-VIMS

G. Filacchione ,[1]★ M. Ciarniello,[1] E. D'Aversa,[1] F. Capaccioni,[1] P. Cerroni,[1] B. J. Buratti,[2] R. N. Clark,[3] K. Stephan[4] and C. Plainaki[5]

[1]*INAF – IAPS, Istituto di Astrofisica e Planetologia Spaziali, Rome, Italy*
[2]*Jet Propulsion Laboratory, California Institute of Technology, Pasadena, CA, USA*
[3]*PSI Planetary Science Institute, Tucson, AZ, USA*
[4]*DLR, German Aerospace Center, Berlin, Germany*
[5]*ASI, Italian Space Agency, Rome, Italy*

Accepted 2020 September 9. Received 2020 September 9; in original form 2020 August 12

ABSTRACT

Photometric correction based on the Shkuratov method is applied to derive visible and infrared albedo maps of Rhea from disc-resolved Cassini VIMS data. Differently from I/F images, albedo maps offer an optimal disentanglement of composition and physical properties of the surface from illumination-viewing effects and to study spectral variations occurring at hemispherical and local scales. A similar methodology has been already applied to Dione's and Tethys's data sets returned by VIMS. Following the same scheme also for Rhea, spectral albedo is derived at 59 wavelengths between 0.35 and 5.047 µm. Equigonal albedo maps are rendered in cylindrical projection with a $0.5^\circ \times 0.5^\circ$ angular resolution in latitude and longitude, corresponding to a maximum spatial resolution of 6.7 km bin^{-1}. Apart from albedo, 0.35–0.55 and 0.55–0.95 µm spectral slopes and the water ice 1.5–2.0 µm band depth maps are computed from photometric-corrected data with the specific scope to investigate the leading-trailing hemisphere colour-albedo dichotomy and to constrain spectral properties above different morphological units including fresh craters (Inktomi) and bright tectonics features (Wakonda-Avaiki Chasmata).

Key words: astronomical instrumentation, methods and techniques: photometric, spectroscopic – planets and satellites: individual: Rhea surface.

1 INTRODUCTION

This letter is the third of a series aiming to the production of photometric corrected maps of Saturn's icy satellites surfaces from Cassini/VIMS data (Brown et al. 2004). After having described the application of the photometric correction method introduced by Shkuratov et al. (2011) to Dione's (Filacchione et al. 2018a) and Tethys's (Filacchione et al. 2018b) data sets, we continue to use a similar methodology for Rhea. In the future, we plan to release similar maps for the remaining Saturn's satellites with the goal to make available common products obtained from the same instrument and with the same processing. These data sets will be valuable for new comparative spectral studies among satellites.

Rhea's surface shows different geological units (Stephan et al. 2012), including: (1) highly cratered terrains; (2) recent and bright impact craters, like Inktomi on the leading hemisphere; (3) very ancient and wide impact basins like Mamaldi–Tirawa on the north-antisaturnian hemisphere; (4) large areas affected by endogenic processes like Avaiki Chasmata, a trough feature extending preferentially along the north–south direction as a result of an extensional fault system developed on the trailing hemisphere (Jaumann et al. 2009). Detailed geologic maps of the Rhea derived from images returned by Cassini ISS have been published by Roatsch et al. (2009, 2012) while global visible colour and albedo maps, photometrically corrected, are provided in Schenk et al. (2011). The ISS maps are rendered at spatial resolution of 1–1.5 km pixel^{-1} above great part of the satellite's surface and they evidence a prominent global asymmetry in both colour and albedo: the darkest and reddest units are in fact observed on the middle of the trailing hemisphere (lon = 270°) interspersed with the bright chasmata pattern while the middle of the leading hemisphere appears brighter and bluer. Due to the tidally locked orbit, the trailing hemisphere of Rhea receives the maximum flux of magnetospheric cold plasma and deposition of small dark particles. In contrast, the leading hemisphere collects the deposition of bright water ice particles from the E ring. Compositional maps of Rhea from VIMS data derived in the past by Stephan et al. (2012) and Scipioni et al. (2014) were computed without applying any specific photometric correction. Nevertheless, these works have enabled the classification of spectral properties observed at hemispheric scale and to establish relationships between spectral classes and geological units at local scales by using simultaneous ISS images. Disc-integrated observations by VIMS, obtained over a wide range of illumination and viewing geometries, have been used to determine Rhea's visible colours and water ice band properties (Filacchione et al. 2007, 2010, 2012). This analysis examines the distribution of chromophores and water ice across Saturn's icy satellites and rings (Filacchione et al. 2013). A combined analysis of UV, visible, and

---

★ E-mail: gianrico.filacchione@inaf.it

infrared data provided geometric albedos of the icy satellites and placed their surface colour variations in relation with the deposition of E-ring particle (Hendrix et al. 2018). Since E ring grains contain a weathered organic material fraction, the observed reddening trend which increases from Enceladus' to Rhea's orbits (Filacchione et al. 2013), could be a consequence of the residence time of the particles in the magnetospheric environment in which the organic material is altered: as a result of this exogenic process, the E ring particles reaching Rhea's surface remain in the magnetosphere for a longer period of time resulting in greater reddening than those falling on the surfaces of the inner moons. To characterize this effect among different moons it is necessary to measure the absolute visible colour reddening of the surfaces by removing the influence of the solar phase angle by means of the photometric correction. At local scales Rhea's surface shows further variability in ices composition. Dalle Ore et al. (2015) have determined the distribution of the relative amounts of crystalline and amorphous water ice on two different impact craters by analysing the distortion of the 2 μm absorption band shape: on the fresh and bright Inktomi crater the maximum crystallinity is ranging between 39 per cent to 67 per cent while on the older Obatala crater they found a lower crystallinity between 31 per cent and 51 per cent. Apart water ice, traces of carbon dioxide ice have been detected by means of the diagnostic band at 4.25 μm which has been observed on the cratered, low albedo terrains of the trailing hemisphere (Stephan et al. 2012).

2 OBSERVATIONS AND DATA SELECTION

VIMS has returned about 720 000 spectra of Rhea's surface during the entire Cassini mission. Since those observations were acquired from a very wide range of distances, illumination, and observation conditions they were not always suitable for photometric analysis and mapping purposes. For this reason, the data set has been mined with the aim to select spectra fulfilling all the following conditions: (1) unsaturated signal ($\leq$4000 DN); (2) incidence angle $i \leq 80^\circ$, emission angle $e \leq 80^\circ$, and phase angle $10^\circ \leq g \leq 120^\circ$; (3) Cassini-Rhea surface distance $\leq$100 000 km, corresponding to a spatial resolution better than 50 km px^{-1} in nominal resolution mode and 17 or 17 × 25 km px^{-1} in high-resolution mode, respectively, for the VIS and IR channels. With respect to previous data selections on Dione's (Filacchione et al. 2018a) and Tethys' (Filacchione et al. 2018b) observations, for Rhea we have extended the maximum phase angle to 120° to improve map coverage. This choice, however, is less reliable to achieve optimal photometric correction like in the previous cases. The filtering conditions are met on a total of about 226 000 spectra which are therefore used to compute photometric correction and maps rendering. Through this filtering, pixels acquired at very oblique views and in the opposition effect regime have been discarded. Observations taken at very low phase angles cannot be corrected by the photometric model we are adopting, as discussed in the next section. VIMS-VIS data are calibrated following the pipeline described in Filacchione (2006) and Filacchione et al. (2007) while VIMS-IR data are calibrated in I/F employing the RC17 pipeline (Clark et al. 2012). The geometry information associated with each VIMS pixel has been derived by a proprietary software based on the reconstructed SPICE kernels (Acton 1996) of the Cassini mission.

3 PHOTOMETRIC CORRECTION

A full description of the photometric correction method is given in Filacchione et al. (2018a) and for sake of brevity is not repeated here. Differently from the methodology previously applied to Dione and Tethys, for which the photometric fit was computed on only 10 wavelengths, for Rhea we have extended the processing on 59 out of the 352 VIMS spectral bands: 14 wavelengths in the visible range ($0.35 \leq \lambda \leq 1.01$ μm) and at 45 in the infrared ($1.047 \leq \lambda \leq 5.047$ μm). These wavelengths are chosen to allow a better computation of the spectral indicators (Section 5) across a wide spectral range. While in principle the photometric correction can be computed at each VIMS band, this operation results very time-consuming and computing intensive. Parameters a, b, and c from fit curves (see equation 5 in Filacchione et al. 2018a) and associated statistical errors are reported in online material table. Parameter a is the equigonal albedo (Shkuratov et al. 2011) or the albedo derived by fitting the distribution of I/F from observations taken at phase angle (g) between 10° and 120° and then extrapolated at null phase ($g = 0^\circ$). Since Shkuratov et al. (2011) theory do not models the opposition sourge effect, the normal albedo $A(\lambda, g = 0^\circ, i = e)$ as defined by Hapke (1993) is higher than the equigonal albedo (a). Since the method is applied to the entire VIMS data set without any specific spatial filtering, the photometric parameters values refer to the average response of Rhea' surface without any distinction between leading and trailing hemispheres or bright and dark terrains. With the adopted method, VIMS data do not allow a reliable retrieval of the photometric parameters at wavelengths affected by low signal-to-noise ratio, like in the strong 3 μm water ice absorption band ($2.866 \leq \lambda \leq 3.029$ μm) and for $\lambda \geq 4.366$ μm where the reflectance is very low. Moreover, the photometric fit fails to converge in the spectral range $3.861 \leq \lambda \leq 4.029$ μm. A similar behaviour is at moment not well understood: a possible cause could be the variability of the continuum level which is temperature dependent in this spectral region, as shown in previous studies on Saturn's satellites and rings (Filacchione et al. 2014, 2016a). Since VIMS observations are acquired at different local times and seasonal period, temperature changes could influence the quality of the photometric fit when applied to the entire VIMS data set. With the exclusion of these restricted spectral ranges, the overall spectral trend appears well-constrained, in particular on the bridging wavelengths between VIMS-VIS (1.010 μm) and VIMS-IR (1.047 μm) channels.

4 ALBEDO MAPS

Equigonal albedo maps of Rhea's surface are created by applying the (1) phase function $F(\lambda, g)$ with the coefficients a, b, c and (2) the disc function $D(i, e, g)$ value as derived from the Akimov model (Shkuratov et al. 1999). Equigonal albedo maps are built employing the method reported in Filacchione et al. (2016a, b): the albedo of each individual VIMS spectrum is projected on the area included within the longitude–latitude positions of the four corners of the pixel. The maps are rendered in simple cylindrical projection with a spatial sampling of 0.5° × 0.5° bin^{-1} corresponding to a spatial resolution of 6.7 km bin^{-1} at the equator of Rhea. In case of data redundancy on a single bin, the median value is shown on the map. In the absence of a detailed global digital shape model of Rhea all the geometry parameters (i, e, g) used in the calculation of the disc function D are computed with respect to the standard spheroid. For this reason, the equigonal albedo maps show illumination residuals in the presence of rough terrains and high craters' rims. Furthermore, we have optimized the choice of (i, e, g) angles within VIMS data set with the scope to maximize the spatial coverage and minimize the correction residuals on extreme illumination/viewing geometries. This method is applied independently for each wavelength and then colour images are rendered by combining different sets of wavelengths as shown in Fig. 1. Noteworthy, the resulting coverage

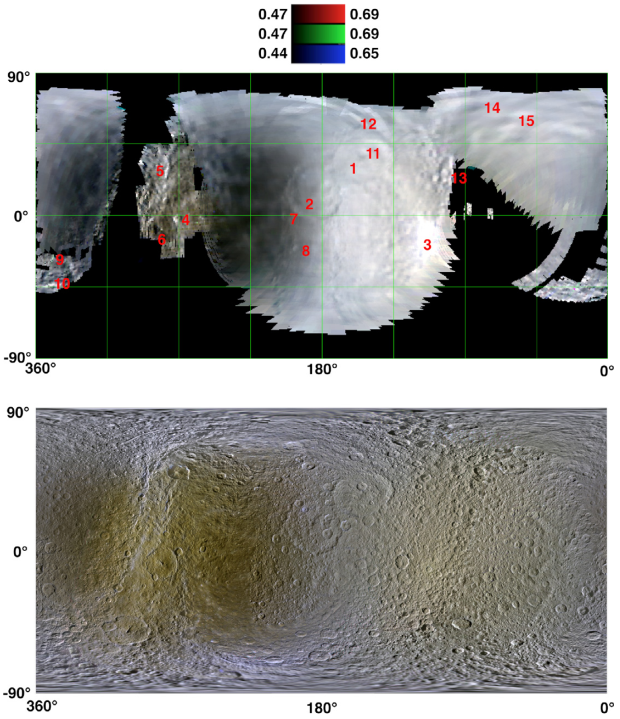

Figure 1. Top panel: Rhea visible colour equigonal albedo map at $B = 0.44$ µm, $G = 0.55$ µm, and $R = 0.7$ µm. Numerals indicate the position of the principal geological features resolved on the map: 1: Tirawa, 2: Mamaldi, 3: Inktomi, 4: Obatala, 5: Wakonda-Avaiki Chasmata, 6: Powehiwehi, 7: Amotken, 8: Utleygon, 9: Qat, 10: Onokoro Catena, 11: Juok, 12: Tuipar, 13: Faro, Adjua, Iraca, 14: Whanin, 15: Ormzad. Bottom panel: Cassini-ISS colour map built by combining IR-Green-UV colour images (Schenk et al. 2011).

between maps taken at different wavelengths could be different to a small degree due to the dissimilar instantaneous field of view in the high-spatial resolution mode and dynamical range of the two VIMS channels. Equigonal maps of Rhea offer a good coverage of both saturnian and antisaturnian regions with some gaps in correspondence of the leading and trailing hemispheres and across the southern latitudes. The visible albedo colour map shown in Fig. 1 – top panel varies between 0.44 and 0.65 at 0.44 µm (band B), and 0.47–0.69 at 0.55 µm (G) and at 0.7 µm (R). VIMS data evidence the albedo dichotomy between the bright leading hemisphere dominated by the fresh ejecta of Inktomi crater (label 3 in Fig. 1) and the dark lens across the trailing hemisphere extending up to ±60° latitudes. The map shows Tirawa (label 1) and Mamaldi (label 2), the two largest impact basins on the North hemisphere of the antisaturnian quadrant and the two smaller craters Amotken (label 7) and Utleygon (label 8) on the transition region of the dark lens. On the apex of the trailing hemisphere at lon = 270° is placed the Wakonda-Avaiki Chasmata (label 5) which extends along the north–south direction and several other impact craters, including the bright rim of Obatala (label 4) and the low albedo floor of Powehiwehi (label 6). The Chasmata region is remarkably brighter than the rest of nearby dark terrains possibly pointing to recent tectonism processes (Stephan et al. 2012). As noted in previous comparisons between VIMS and ISS visible albedo maps (Schenk et al. 2011) for Dione (Filacchione et al. 2018a) and Tethys (Filacchione et al. 2018b), the ISS Rhea map (Fig. 1b) likewise appears more uniform in photometric rendering and more resolved than the VIMS one. This is consequence of: (1) the higher spatial resolution of ISS images (IFOV = 6–60 µrad pixel^{-1}, Porco et al. 2004) with respect VIMS hyperspectral data (IFOV = 166 to 500 μrad pixel^{-1}, Brown et al. 2004); (2) the different filtering of the phase angle range chosen to process ISS and VIMS images. In fact, the ISS albedo map is preferentially derived from images collected in a small phase angle range (from 10° to 30°) after applying simplified Lunar–Lambertian photometric correction (McEwen 1991). Conversely, the VIMS map is built from observations taken in a more wide (10°–120°) phase angle range. This choice has been dictated by the need to maximize the spatial coverage. Despite the VIMS data are processed with a mathematical photometric correction, the resulting albedo map appears progressively less accurate at extreme illumination and viewing angles. In these conditions some photometric residuals appear on the map like on the region at about lon = 240° eastwards the Obatala crater (label 4 in Fig. 1– top panel) where the colour rendering does not perfectly match across the seam. The result of the photometric correction applied to six infrared wavelengths (1.01, 1.54, 1.82, 2.05, 2.20, and 3.81 µm) is shown in online material figure. We have selected a combination of continuum (1.01, 1.82, 2.20, and 3.81 µm) and water ice absorption bands (1.54, 2.05 µm) to derive the infrared albedo of bright and dark terrains and then to compute water ice band depths as discussed in the next Section 5. The contrast between the bright leading and the dark trailing hemisphere can be appreciated only on the 1.01 and 3.81 µm maps whereas on the remaining wavelengths maps the albedo maps appear much more uniform between the two hemispheres. In the next section, we discuss how spectral indicators are computed starting from equigonal albedo data.

5 SPECTRAL INDICATORS MAPS

The four visible and infrared spectral indicators maps are computed from albedos following the method discussed in Filacchione et al. (2012). In Fig. 2 are shown the 0.35–0.55 and the 0.55–0.95 µm spectral slope and the 1.5–2.0 µm water ice band depth. In previous studies (Filacchione et al. 2007, 2010, 2012, 2013, 2014; Ciarniello et al. 2011), we have discussed how these spectral indicators are suitable to trace the relative amounts of compositional end members (water ice and chromophores) and surface regolith grain size. The 0.35–0.55 µm slope map (Fig. 2 – top left panel) traces the leading-trailing dichotomy with a great contrast: the slope reaches the maximum reddening (1.0 1/µm) across the leading hemisphere in the Tirawa and Inktomi craters neighbourhood and on the apex of the trailing hemisphere in correspondence of the Wakonda–Avaiki Chasmata bright terrains and Obatala–Powehiwehi craters. On the rest of the dark terrains of the trailing hemisphere, including Qat crater and Onokoro Catena, the reddening is minimum reaching a spectral slope as low as 0.5 1/µm. The transition region across the antisaturnian meridian (lon = 180°), where Mamaldi, Amotken and Utleygon craters are located, is characterized by intermediate slope (0.75 1/µm). As a consequence of this spatial distribution of the spectral slope, the colours of the two largest and ancient impact basins, i.e. Tirawa and Mamaldi, appear significantly different: the former is in fact more red coloured than the latter. Contrary to the 0.35–0.55 µm slope spatial distribution, the 0.55–0.95 µm slope appears much more uniform across Rhea's surface (Fig. 2 – bottom left panel). The maximum reddening (0.07 1/μm) is observed again on the apex of the trailing hemisphere whereas null to positive slopes are uniformly measured across the equatorial regions. The minimum slope, corresponding to a bluing of −0.12 1/µm, is reached on the antisaturnian quadrant at latitudes ≥±45°. Water ice band depths

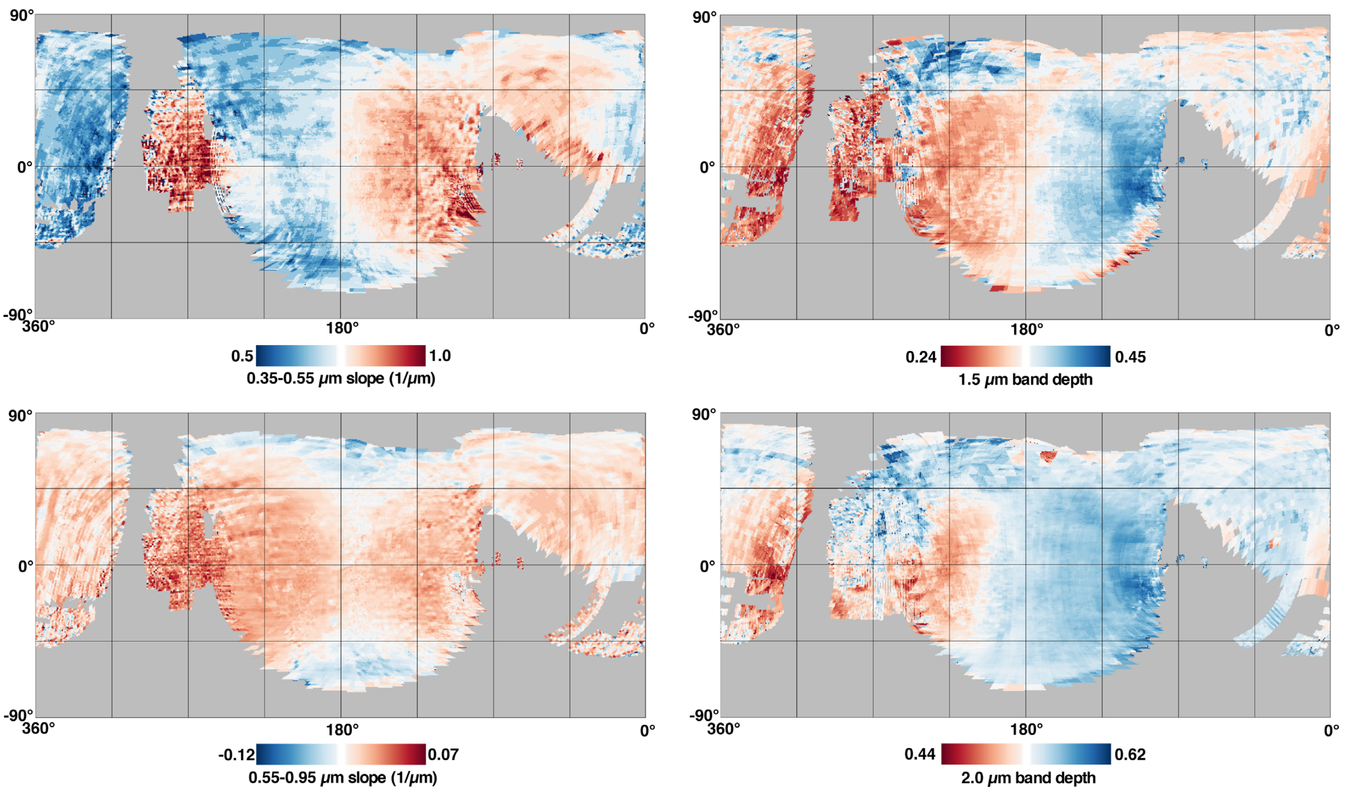

Figure 2. Rhea cylindrical maps for 0.35–0.55 μm slope (top left panel), 0.55–0.95 μm slope (bottom left panel) and 1.5 μm water ice band depth (top right panel) and 2.05 μm band depth (bottom right panel).

at 1.5 μm (Fig. 2 – top right panel) and at 2.0 μm (Fig. 2 bottom right panel) show a similar behaviour in many areas: the maximum band depth is reached on the Inktomi crater and nearby ejecta where BD(1.5 μm) = 0.45 and BD(2.0 μm) = 0.62. Another region of intense 1.5–2.0 μm band depth values is located in the area between 180° ≤ lon ≤ 270° at lat ≥ +45°. The two maps show a different behaviour on the high albedo units placed at the apex of the trailing hemisphere in correspondence of the Wakonda-Avaiki Chasmata bright terrains and Obatala–Powehiwehi craters where the 1.5 *μ*m band depth decreases much more than the 2.0 *μ*m band depth. The minimum band depth values are in general measured across the dark terrain of the trailing hemisphere. Photometric residues are visible on the points at the southern edge of the antisaturnian hemisphere.

6 DISCUSSION AND CONCLUSIONS

In this study, we show how photometrically corrected spectral maps of Rhea rendered at 6.7 km bin^{-1} resolution are suitable to study the spatial distribution of visible to near-infrared albedo and spectral indicators across the surface of the moon. In general, we observe a strong spatial correlation among albedo, visible colours and water ice band depth distributions: the bright terrains on the leading hemisphere are characterized by the maximum water ice band depth and the more intense reddening while the dark terrains placed on the trailing hemisphere are associated with the minimum water ice band depth and less intense reddening. This large-scale dichotomy between the two hemispheres is mainly driven by exogenic processes. In fact, the leading hemisphere is affected by the deposition of E-ring particles contributing to the accumulation of a layer of fine grained and bright water ice particles (Schenk et al. 2011). The intense water ice band depth values rendered in light blue colour in Fig. 2 – right column, are compatible with grain sizes of the order of tens of microns (Filacchione et al. 2012). A striking spectral difference with respect to the rest of the leading hemisphere is visible on the 48 km-wide Inktomi crater (label 3 in Fig. 1), probably the most recently formed large crater in the Saturn system (Wagner et al. 2007; Dones et al. 2009). A bright ray system extends from the crater for several hundreds of kilometres. Across the neighbourhood region we measure the highest visible albedo (0.65 at B = 0.44 μm, 0.69 at G = 0.55 μm, and R = 0.7 μm) correlated with very high spectral slopes (0.07 1/μm for the 0.35–0.55 μm slope) and very high water ice bands depths (marked in dark blue colour in Fig. 2 – right column, and corresponding to 0.45 and 0.62 for the 1.5 and 2.0 μm bands, respectively). Assuming pure water ice composition, similar band depths values are compatible with sub-cm to centimetre grain sizes (see fig. 6 in Filacchione et al. 2012) associated with the ejecta blanket. The high reddening measured through the 0.35–0.55 μm slope on this same area could be explained by the presence of small quantities of contaminants/darkening agents bound at intramolecular level with the water ice during the impact. A similar behaviour, e.g. concurrent high reddening and high band depths, is not unusual since it has been already observed on the brightest regions of Saturn's A and B rings where the particles are experiencing a continuous mixing of their materials caused by collisions (Nicholson et al. 2008; Cuzzi et al. 2009; Hedman et al. 2013; Filacchione et al. 2014; Ciarniello et al. 2019). We report that the blue spots located at lon = 130° lat = 0° observed by Schenk et al. (2011) on Cassini ISS images (530 m pixel^{-1} resolution) are not recognizable on VIMS maps (6.7 km bin^{-1}) probably due to the lower spatial resolution; further spots recognizable at lon = 79° lat = 0° on ISS images are not covered on VIMS map. Since a tenuous ring has been reported around Rhea (Jones et al. 2008a, b) these spots have been speculated to be impact sites of circum-satellite material fallen on to the surface along Rhea's equator. Moving to the trailing hemisphere surface, we observe that it appears in general darker due to the bombardment of magnetospheric particles and dark dust grains. Dark terrains appear chemically processed by radiolysis induced by charged particles. A similar process can induce the formation of several byproducts capable to alter the surface composition, from simple organic matter when water ice is irradiated by C^+ and N^+ magnetospheric ions (Johnson 1996) to the formation of CO_2 ice from irradiation of water ice and carbon-bearing minerals (Moore et al. 1983). In fact previous studies based on VIMS data have evidenced the presence of a faint band at 4.25 µm caused by CO_2 ice bound to the low albedo ices as a consequence of the larger availability of carbon rich materials (Clark et al. 2008; Stephan et al. 2012). Apart organic matter, other compounds like amorphous silicates (Poulet et al. 2003), carbonaceous particles (Cuzzi & Estrada 1998), nanophase iron or hematite (Clark et al. 2008), tholins intimately mixed in water ice grains (Ciarniello et al. 2011), or combinations of these materials (Cuzzi et al. 2018; Ciarniello et al. 2019) act as chromophores altering the visible colours and inducing a moderate to positive (or red) spectral slope at visible wavelengths. This general trend across the trailing hemisphere shows few local exceptions associated with endogenous processes. On the apex of the trailing hemisphere ($\mathrm{lon} = 270^\circ$) are located the wispy terrains of Wakonda-Avaiki Chasmata. This area is remarkably different with respect to the rest of the trailing hemisphere being brighter (see albedo map in Fig. 1) and less red coloured (see 0.35–55 µm slope map in Fig. 2 – top left panel). The two water ice band depth maps show a different behaviour: at 1.5 µm (Fig. 2 – top right panel) the chasmata is similar to the near terrains while on the 2-µm band depth map (same figure, bottom right panel) it is less intense. Geomorphological analyses have shown that the Chasmata is formed by extensional tectonism resulting in the resurfacing of more fresh material. This would explain the higher albedo and less intense reddening though in correspondence of rough topography we need to be careful because possible residuals could affect the photometric correction. After having derived photometrically corrected VIMS data sets for Dione, Tethys, and Rhea we plan for the future to use a similar methodology to the remaining regular satellites (Mimas and Enceladus). The final aim of this work is to derive compositional maps of Saturn's icy satellites by applying a common spectrophotometric correction to Cassini-VIMS data set.

ACKNOWLEDGEMENTS

We thank Dr. Paul Helfenstein for the thorough review of the manuscript. The authors acknowledge the financial support from the Italian Space Agency (ASI) for the Cassini-VIMS data analysis program. This research has made use of NASA's Astrophysics Data System.

DATA AVAILABILITY STATEMENT

All data used in this work are publicly available through NASA-PDS at `https://pds-imaging.jpl.nasa.gov/volumes/vims.html`. The analysis discussed in this paper has been made by using proprietary software developed in the IDL-ENVI language by the authors. Albedo and spectral indicators maps will be shared on reasonable request to the corresponding author.

REFERENCES

Acton C., 1996, Planet Space Sci., 44, 70
Brown R. H. et al., 2004, Space Sci. Rev., 115, 111
Ciarniello M. et al., 2011, Icarus, 214, 541
Ciarniello M. et al., 2019, Icarus, 317, 242
Clark R. N. et al., 2008, Icarus, 193, 372
Clark R. N. et al., 2012, Icarus, 218, 831
Cuzzi J. N., Estrada P. R., 1998, Icarus, 132, 1
Cuzzi J. N., et al., 2009, in Dougherty M. et al., Saturn from Cassini-Huygens. Springer Science+Business Media B.V., Dordrecht, p. 459
Cuzzi J. N. et al., 2018, Icarus, 309, 363
Dalle Ore C. M. et al., 2015, Icarus, 261, 80
Dones L. et al., 2009, in Dougherty M. et al., Saturn from Cassini-Huygens. Springer Science+Business Media B.V., Dordrecht, p. 613
Filacchione G. et al., 2007, Icarus, 186, 259
Filacchione G. et al., 2010, Icarus, 206, 507
Filacchione G. et al., 2012, Icarus, 220, 1064
Filacchione G. et al., 2013, ApJ, 766, 5
Filacchione G. et al., 2014, Icarus, 241, 45
Filacchione G. et al., 2016a, Icarus, 271, 292
Filacchione G. et al., 2016b, Icarus, 274, 334
Filacchione G. et al., 2018a, Geophys. Rev. Lett., 45, 2184
Filacchione G. et al., 2018b, Geophys. Rev. Lett., 45, 6400
Filacchione G., 2006, PhD thesis. Univ. Napoli Federico II
Hapke B., 1993, Theory of Reflectance and Emittance Spectroscopy. Cambridge Univ. Press, Cambridge, UK
Hedman M. M. et al., 2013, Icarus, 223, 105
Hendrix A. R. et al., 2018, Icarus, 300, 103
Jaumann R. et al., 2009, in Dougherty M. , et al., Saturn from Cassini-Huygens. Springer Science+Business Media B.V.,, Dordrechtp. 637
Johnson R. E., 1996, Rev. Mod. Phys., 68, 305
Jones G. H. et al., 2008a, Eos Trans. AGU, American Geophysical Union, Fall Meeting,
Jones G. H. et al., 2008b, Science, 319, 1380
McEwen A., 1991, Icarus, 92, 298
Moore M. H. et al., 1983, Icarus, 54, 388
Nicholson P. D. et al., 2008, Icarus, 193, 182
Porco C. C., 2004, Space Sci. Rev., 115, 363
Poulet F. et al., 2003, A&A, 412, 305
Roatsch T. et al., 2015, PSS, 61, 135
Roatsch T., Jaumann R., Stephan K., Thomas P. C., 2009, in Dougherty M., ed. Saturn from Cassini-Huygens. Springer Science+Business Media B.V., Dordrecht.p. 763
Schenk P. et al., 2011, Icarus, 211, 740
Scipioni F. et al., 2014, Icarus, 234, 1
Shkuratov Y. et al., 1999, Icarus, 137, 235
Shkuratov Y. et al., 2011, Planet Space Sci., 59, 1326
Stephan K. et al., 2012, Planet. Space Sci., 61, 142
Wagner R. et al., 2007, EOS, 87

SUPPORTING INFORMATION

Supplementary data are available at *MNRASL* online.

Figure S1 Rhea infrared albedo maps at 1.01, 1.54, 1.82, 2.05, 2.20, and 3.81 µm (from top left to bottom right panel).

Table S1 Photometric fit parameters (a,b,c) derived for the 59 visible-infrared wave- lengths of VIMS. The parameter a corresponds to the equigonal albedo value.

This paper has been typeset from a TEX/LATEX file prepared by the author.